Electronic Supplementary Material (ESI) for Energy & Environmental Science.

Supplementary Information

Highly Efficient Photocatalytic H_2O_2 Production in Microdroplets: Accelerated Charges Separation and Transfer at Interface

Kejian Li[a, b], Qiuyue Ge[a], Yangyang Liu[a], Longqian Wang[a], Kedong Gong[a], Juan Liu[a], Lifang Xie[a], Wei Wang[a], Xuejun Ruan[a], Liwu Zhang[a, b, c *]

[a] Department of Environmental Science and Engineering, Fudan University, Shanghai 200433, People's Republic of China

[b] Shanghai Key Laboratory of Atmospheric Particle Pollution and Prevention, Fudan University, Shanghai 200433, People's Republic of China

[c] Shanghai Institute of Pollution Control and Ecological Security, Shanghai 200092, People's Republic of China

* Corresponding author E-mail: zhanglw@fudan.edu.cn

Supplementary Methods

Materials

Melamine, triethanolamine (TEOA), acetone, H_2O_2 (30%), NaOH, HCl (36%~38%), NaCl, NaBr, Na_2SO_4, and $FeSO_4\cdot 2H_2O$ were all of analytic grade and purchased from Sinopharm Group Co., Ltd. ZnO (99.9% metals basis, 30 ± 10 nm), anatase TiO_2 (99.8% metals basis, 25 nm), NaSCN, and $HAuCl_4\cdot 3H_2O$ (99.9%) were supplied by Aladdin Reagents Co., Ltd. Potassium titanium oxalate (PTO, $K_2TiO(C_2O_4)_2\cdot H_2O$, 99%) and methyl orange (MO, 98%) were obtained from Macklin. CAB-O-SIL TS720 (Hydrophobic (alkyl treated) fumed silica) was purchased from Cabot Corp., Boston, MA. Deionized (DI) water with specific resistance $\geq$ 18.2 MΩ cm was used throughout the whole experiments. The hydrophobic treatment was achieved via immersing the pre-cleaned quartz wafer in CAB-O-SIL TS720 in acetone suspension (10 g L^{-1}) for 4 min and then dried at 80 °C for 5 h.

Photocatalysts Preparation

g-C_3N_4 nanosheets preparation:[1, 2] Typically, 10 g melamine was first calcinated at 520 °C in air for 4 h with a ramping rate of 2.3 °C min^{-1}, and then the yellow bulk particles were further heated at 550 °C for 2 h and ground into fine powder. The *g*-C_3N_4 nanosheets were finally obtained by ultrasonication exfoliation of the as-prepared powderS. In detail, the as-synthesized g-C_3N_4 powder (0.1 g) was added into 500 mL deionized water in a glass beaker. After high-powered ultrasonication treatment under stirring for 10 h, the suspension was left standing for 24 h to make aggregates settle naturally. Then, the upper highly-stable dispersion with *g*-C_3N_4 nanosheets mass concentration of 0.086 g L^{-1} was transferred to a blue cap bottle for later use.

Au/TiO_2 and Au/ZnO nanoparticles synthesis:[3] Au nanocrystals (4 wt.%) were loaded on commercial TiO_2 and ZnO nanoparticles by deposition-precipitation method. Typically, 40 mg $HAuCl_4\cdot 4H_2O$ was dissolved in 200 mL DI water and the solution pH was adjusted to 7 using 0.1 M NaOH. 1 g TiO_2 (or ZnO) was then added into the solution and the suspension was vigorously stirred at 70 °C for 2 h. The mixture was centrifuged and washed with copious amount of DI water and dried under vacuum at 60 °C. The resulting powder was further calcined at 400 °C for 4 h in air with a heating rate of 3 °C min^{-1}. In order to obtain quasi-homogenous suspensions containing TiO_2, Au/TiO_2, ZnO and Au/ZnO nanocatalysts, the treatment method is the same as that for g-C_3N_4

nanosheets. The corresponding mass concentrations were 0.33, 0.09, 0.37 and 0.17 g L^{-1}.

Characterizations

The XRD patterns were recorded using X-ray diffractometer (Bruker D8 Advance, XRD) with Cu Kα radiation for crystal structures analysis. The accelerating voltage and operating current were 40 kV and 40 mA, respectively. The morphology structure was characterized by high-resolution transmission electron microscopy (HRTEM, FEI Tecnai F20, Japan). The UV-vis diffuse reflectance spectra were recorded using a UV-vis spectrophotometer (UV-2600, Shimadzu, Japan) and $BaSO_4$ was used as reference. The band gap energy (E_g) was obtained from the plot of $(\alpha h v)^n$ versus hv, where hv presents light energy, α means the measured light absorption coefficient, and n = 1/2 for g-C_3N_4 and n = 2 for TiO_2 and ZnO.[4-6] The valence band X-ray photoelectron spectroscopy (VB XPS) was measured using Thermo Scientific K-Alpha. The Zeta potentials of the employed photocatalysts were measured using Malvern Zetasizer Nano ZS90 at initial pH of the as-prepared photocatalyst suspensions (the detected pH value of g-C_3N_4, TiO_2, Au/TiO_2, ZnO, and Au/ZnO suspension is 7.13, 6.21, 6.75, 7.82, and 7.11, respectively). In addition, the zeta potentials of g-C_3N_4 nanosheets were also measured at alkaline pH, adjusted using TEOA.

Details on ink-jet printing for microdroplet generation

In order to obtain microdroplets with pre-designed diameters of about 165, 240, 345, 415, 515, and 590 μm, the printing times at a same position were adjusted to 33, 100, 300, 520, 1000, and 1500, respectively. The corresponding microdroplets arrays generated in a hydrophobic quartz wafer were 35 × 35, 30 × 30, 25 × 25, 20 × 20, 20 × 20, and 15 × 15, where numbers represent the number of rows and columns. To inhibit water evaporation during printing, a stainless-steel ice cube was placed underneath the hydrophobic quartz wafer and 35% relative humidity was controlled. However, at present, the investigations on photocatalysis in microdroplets with size less than 100 μm are difficult due to the limitations on microdroplets generation, collection, and further precise analyses.

Hydrogen peroxide measurements

H_2O_2 concentration was measured using PTO and spectrophotometric analysis method (denoted as PTO method).[7] It is worth noting that TEOA can react with pertitanic acid (a product from the chromogenic reaction between PTO and H_2O_2), leading to a lower detection value than the true one (Fig. S31). Therefore, the interferences of TEOA on H_2O_2 detection should be considered and eliminated. It was found that the low concentration TEOA (< 2 mM) shows negligible influence on H_2O_2 determination (Fig. S32), thus, the TEOA concentration in microdroplet system was diluted to < 2 mM based on the initial concentration. The spectrophotometric analysis was performed by adding 400 μL of 0.1 M PTO into 1.2 mL aliquot, and the absorbance at 400 nm was measured using a Shimadzu UV-vis spectrometer after 5 min. The calibration curve was established with the identical procedure using H_2O_2 standard solution without adding TEOA (Fig. S33). However, for bulk phase reaction, it is infeasible to dilute TEOA owing to the low H_2O_2 production and high detection limit. To simplify, the concentration change of TEOA during photocatalytic reaction was not considered because of the high initial concentration. Hence, for bulk phase H_2O_2 concentration measurement, standard curves were established in the presence of TEOA with different concentrations (400 μL of 0.1 M PTO and 1.2 mL H_2O_2 solution containing TEOA). As a result, the H_2O_2 production in bulk phase reaction was overestimated to some extent.

Moreover, in order to confirm the detected H_2O_2 concentration, another color development method with addition of potassium iodide (KI) and ammonium molybdate ($(NH_4)_2MoO_4$) (denoted as $KI^-(NH_4)_2MoO_4$ method) was employed.[8] In detail, 0.5 mL of reacted sample was mixed with 1 mL 0.1 M KI and 0.025 mL 0.01 M $(NH_4)_2MoO_4$, and the absorbance at 350 nm was recorded after 5 min. The established calibration curve was shown in Fig. S34. The experimental results (Fig. S35) showed that detected concentration of H_2O_2 generated from microdroplet photocatalysis using PTO method and $KI^-(NH_4)_2MoO_4$ method was almost identical, verifying that the reported H_2O_2 concentrations were credible.

DO and ESR measurements

The dissolved oxygen (DO) concentration was measured during bulk phase photocatalysis with an optical dissolved oxygen measuring instrument (Multi 3620IDS, Xylem Analytics Co., Ltd., Germany) that was immersed in solution. The electron spin resonance measurements of superoxide radicals ($O_2^{\bullet-}$) with DMPO as spin trapper were carried out in methanol solution containing g-C_3N_4 nanosheets in the presence and absence of O_2 bubbling.

In-situ application tests

The Fenton reaction was conducted to explore the *in-situ* applicability of microdroplet photocatalytic H_2O_2 production. Here, g-C_3N_4 nanosheets and Au/ZnO nanoparticles were employed as photocatalysts for H_2O_2 production (50 mM TEOA, light irradiation intensity 3.15 mW cm^{-2}, 2 h irradiation). The microdroplet photosynthesis was carried out for four times to obtain sufficient sample for further usage (denoted as m-H_2O_2), and the bulk phase reaction was repeated twice (named as b-H_2O_2). m-H_2O_2 was diluted 3 times for Fenton reaction while b-H_2O_2 was directly used. Methyl orange (MO) degradation was applied to estimate the Fenton reaction efficiency (Experimental parameters: Fe^{2+} concentration, 5 mM; initial pH, 2.8; MO concentration, 70 mg L^{-1}; reaction time 5 min). The concentration of MO was measured using UV-vis spectrophotometer and the MO degradation efficiency (DE_{MO}) was calculated using equation (S1).

$$DE_{MO} = (1 - C_t/C_0) \times 100\% \qquad \text{(eq. S1)}$$

Where C_t and C_0 is the MO concentration at reaction time t and the initial one, respectively.

Electric field measurements

The microdroplet electric field was experimentally measured with the help of vibrational Stark effect using micro-Raman spectroscopy, because the Raman shift of C≡N bond (*v*(C≡N)) is highly sensitive to external electric field.[9] In the experiments, microdroplets containing NaSCN and Au nanoparticles were used for micro-Raman measurements because the strong chemical adsorption between SCN^- and Au nanoparticles that are of surface-enhanced Raman scattering property could improve electric field response and signal-to-noise ratio.[10-12] Au nanoparticles were prepared following previous study.[13]

The bulk solutions were prepared by mixing 2 M NaSCN and 500 μL of as-synthesized Au nanoparticles suspension (diameter ~50 nm, TEM image shown in Fig. S36) without and with addition of 0.2 M NaCl or 0.2 M Na_2SO_4. The microdroplets were sprayed onto superhydrophobic quartz wafer, which was then placed in a flow cell that used for *in-situ* photocatalytic H_2O_2 decomposition measurement (Fig. S29), and high-purity air with high relative-humidity was purged into to inhibit water evaporation. The Raman spectra assigned to *v*(C≡N) were recorded in microdroplet interior and interfacial region. The Raman signal was collected using a multichannel

EMCCD device ranged from 2000-2180 cm^{-1} after 785 nm laser excitation, with 2 spectrum accumulations at a 20 s acquisition time per spectrum. The electric field strength (E) is calculated from the following conversion equation (eq. S2):[10]

$$E = (\Delta\nu(C{\equiv}N)/0.36) \times 10^6\ [(V/cm)/cm^{-1}] \quad \text{(eq. S2)}$$

where $\Delta\nu(C{\equiv}N)$ is the difference value of detected Raman shift of $\nu(C{\equiv}N)$ between microdroplet interior and air-water interface.

Photocatalytic stability tests

To investigate the stability of catalytic activity after photocatalytic reactions, the microdroplet photocatalysis was performed for several times to collect sufficient suspension without dilution for further experiments. After that, the photocatalysts were separated from aqueous solution through high-speed centrifugation at 10000 rpm for 10 min and washing with DI water. Then the photocatalysts were rediapered into the same volume of DI water containing TEOA as before centrifugation via ultrasonication for 5 min. The microdroplet photocatalysis was carried out following the previously described procedures.

Density functional theory calculations

First-principles calculations were carried out on the basis of periodic DFT using a generalized gradient approximation within the Perdew-Burke-Ernzerhof exchange correction function.[14, 15] We used the projector-augmented wave method for describing ionic cores as implemented in the Vienna ab initio simulation package (VASP). For the microdroplet system, the solid/liquid interfaces were calibrated with VASPsol code. The EB_K is set to 80. The wave functions were constructed from the expansion of plane waves with an energy cutoff of 450 eV. An optimized supercell of nitrogen-bridged heptazine was adopted as pristine g-C_3N_4 model for calculation (Fig. S37). Gamma centered k-piont of 3×3×1 have been used for the geometry optimization. The consistence tolerances for the geometry optimization are set as 1.0×10^{-5} eV/atom for total energy and 0.05 eV/Å for force, respectively. In order to avoid the interaction between the two surfaces, a large vacuum gap of 15 Å has been selected in the periodically repeated slabs.

Some reactions adopted for calculation of each step were shown as follows:[16, 17]

$$O_2 + * \rightarrow *O_2 \quad \text{(eq. S3)}$$

$$*O_2 + H^+ + e^- \rightarrow *OOH \quad \text{(eq. S4)}$$

$$*OOH + H^+ + e^- \rightarrow *H_2O_2 \quad \text{(eq. S5)}$$

$$*H_2O_2 \rightarrow H_2O_2 + * \quad \text{(eq. S6)}$$

According to previous reports, the adsorption energy of O_2 was calculated using following equation:

$$E_{\mathrm{ads}}(O_2) = E(*O_2) - E(*) - E(O_2) \quad \text{(eq. S7)}$$

Where $E(*O_2)$, $E(*)$, and $E(O_2)$ represent the total energy of sample with surface adsorbed O_2, the energy of pristine g-C_3N_4, and O_2 molecule, respectively.

Besides, the Gibbs reaction free energy of each step was calculated using following equation:

$$G(\mathrm{T}) = E_{\mathrm{ele}} + G_{\mathrm{corr}}(\mathrm{T}) = E_{\mathrm{ele}} + \mathrm{ZPE} + \mathit{\Delta} G_{0\text{-T}} \quad \text{(eq. S8):}$$

where E_{ele}, $G_{\mathrm{corr}}(\mathrm{T})$, ZPE and $\mathit{\Delta} G_{0\rightarrow \mathrm{T}}$ were electronic energy, thermal corrections to Gibbs free energy, zero-point energy and contribution by heating the system from 0 K to 298 K.

AQY and STH calculation

The apparent quantum yield (AQY) of H_2O_2 photocatalytic production was calculated using the following equation:[18, 19]

$$\mathrm{AQY} = (2 \times [H_2O_2] \times \mathrm{V} \times N_A) / (\mathrm{IS}t\lambda/hc) \quad \text{(eq. S9)}$$

The solar-to-chemical conversion efficiency (STH) was determined using following equation:

$$\mathrm{STH} = \Delta G(H_2O_2) \times [H_2O_2] \times \mathrm{V} / (\mathrm{IS}t) \quad \text{(eq. S10)}$$

where $[H_2O_2]$ is the generated H_2O_2 concentration, V is volume of suspension, I is the incident light irradiation intensity (23.2 W m^{-2}), S is the irradiation area, t is the reaction time (3600 s), h is Planck’s constant (6.63×10^{-34} m^2 kg s^{-1}), λ is the incident light wavelength (365 nm), c is the speed of light in free space (3.0×10^8 m s^{-1}), N_A is the Avogadro's constant (6.02×10^{23} mol^{-1}), $\Delta G(H_2O_2)$ is the free energy of H_2O_2 formation (117 kJ mol^{-1}).

Electric field simulations

The electric field in microdroplet of varying diameter was simulated according to a simple model proposed by Zare et al.,[20] in the case of singly charged species in a microdroplet with ions concentration of 1×10^{-6} M. Owing to the scope of application of the calculation model, the electric field simulation was mainly carried out in smaller microdroplets.

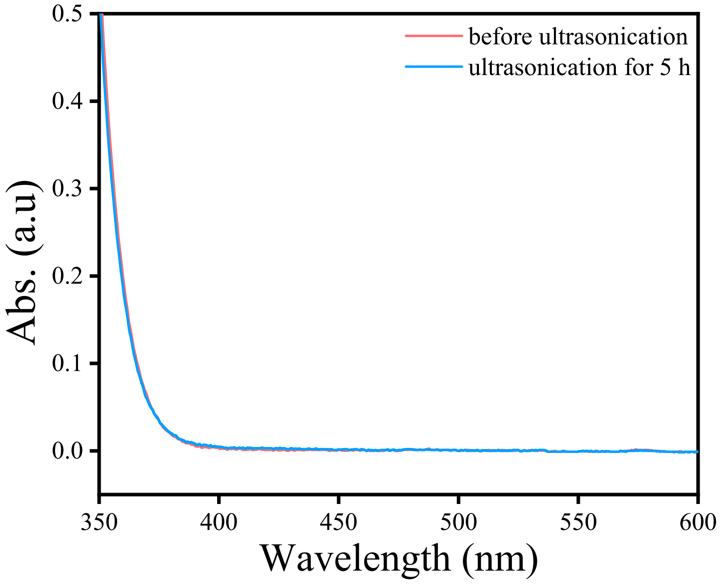

Fig. S1. The UV-vis absorption spectra of g-C_3N_4 photocatalyst suspension after filtration in the presence of PTO before and after ultrasonication for 5 h.

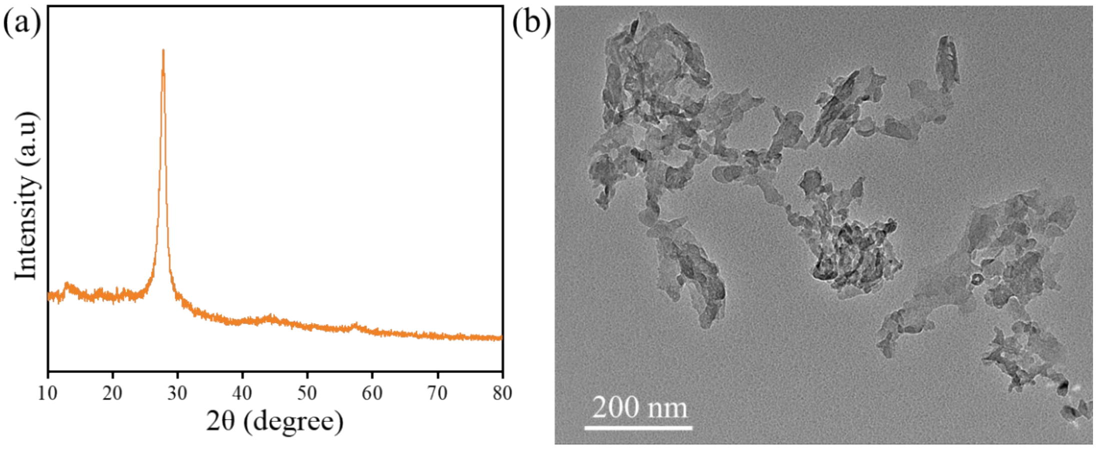

Fig. S2. (a) XRD pattern and (b) TEM image of g-C_3N_4 nanosheets.

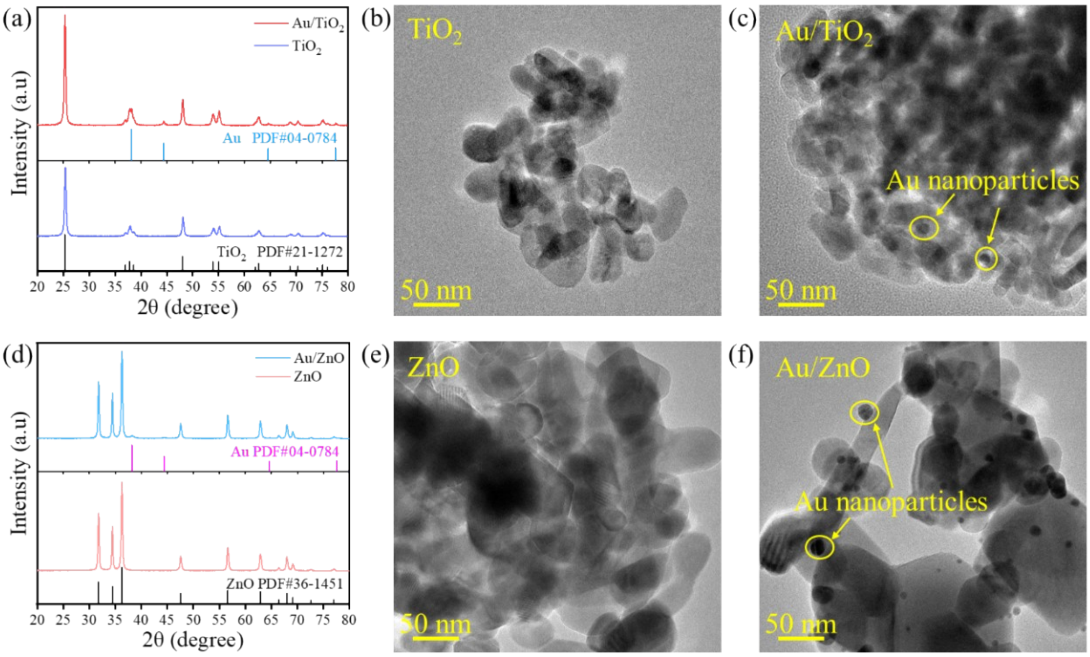

Fig. S3. XRD patterns and TEM images of TiO_2, Au/TiO_2, ZnO, and Au/ZnO nanoparticles.

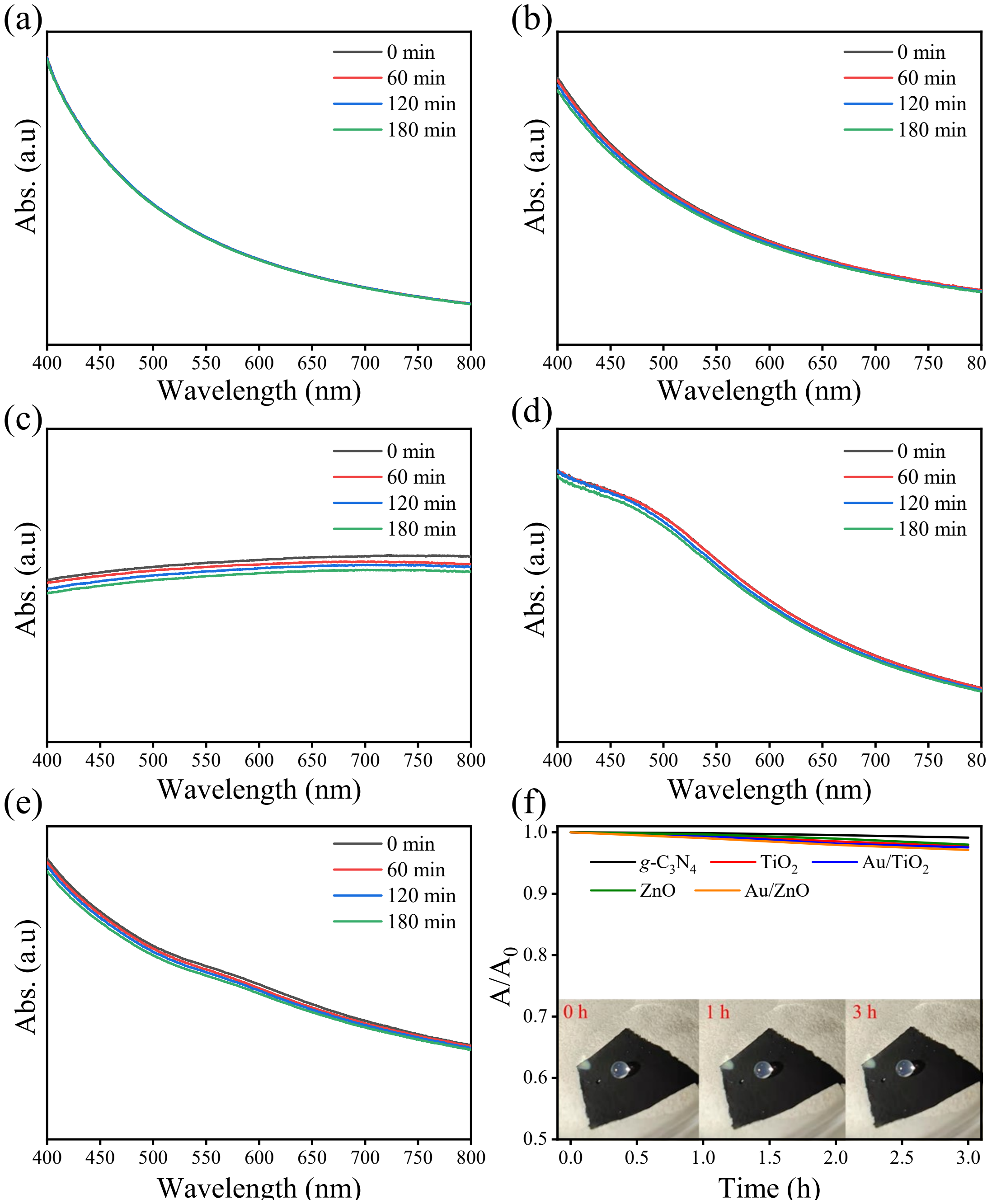

Fig. S4. (a-e) The measured UV-vis absorption spectra of as-prepared photocatalyst suspensions containing g-C_3N_4, TiO_2, Au/TiO_2, ZnO, and Au/ZnO, respectively. (f) Settling curves of the as-prepared photocatalyst suspensions. The insets are photos of a droplet containing g-C_3N_4 nanosheets at different time.

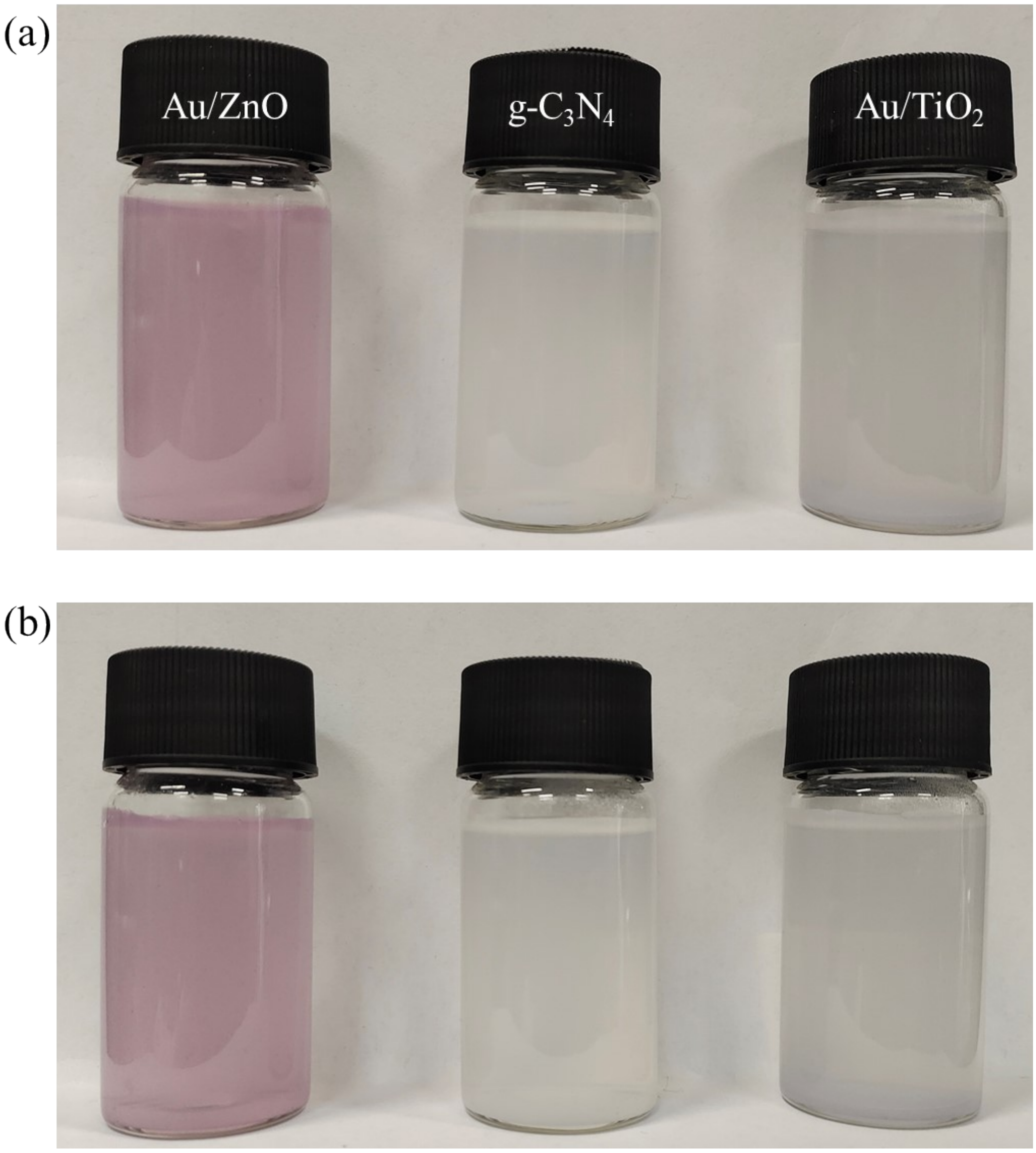

Fig. S5. Photos of the as-prepared highly-stable nanocatalysts suspensions. (a) before and (b) after 7 days.

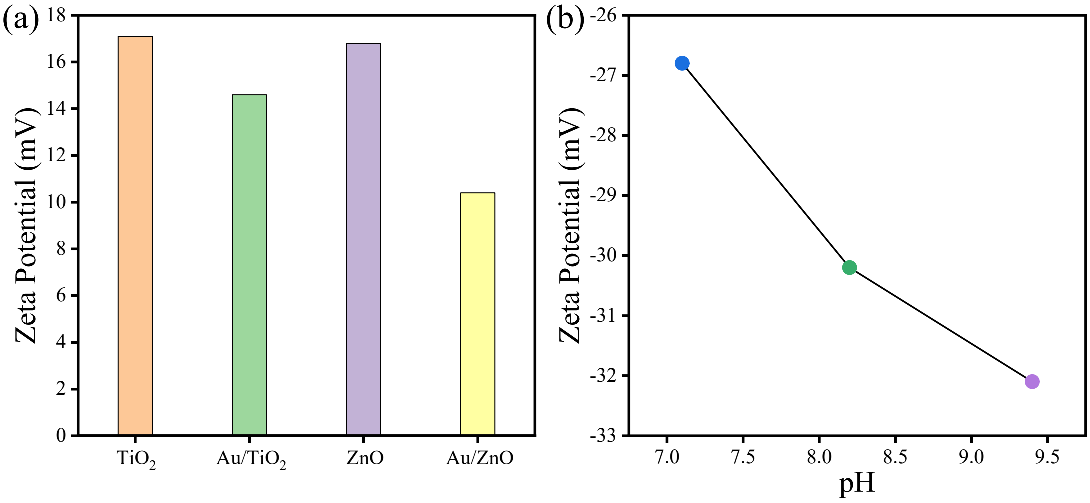

Fig. S6. (a) The detected zeta potentials of TiO$_2$, Au/TiO$_2$, ZnO, and Au/ZnO nanoparticles at initial pH of the as-prepared photocatalyst suspension. (b) The detected zeta potentials of g-C$_3$N$_4$ nanosheets suspension at different pH values, adjusted using TEOA.

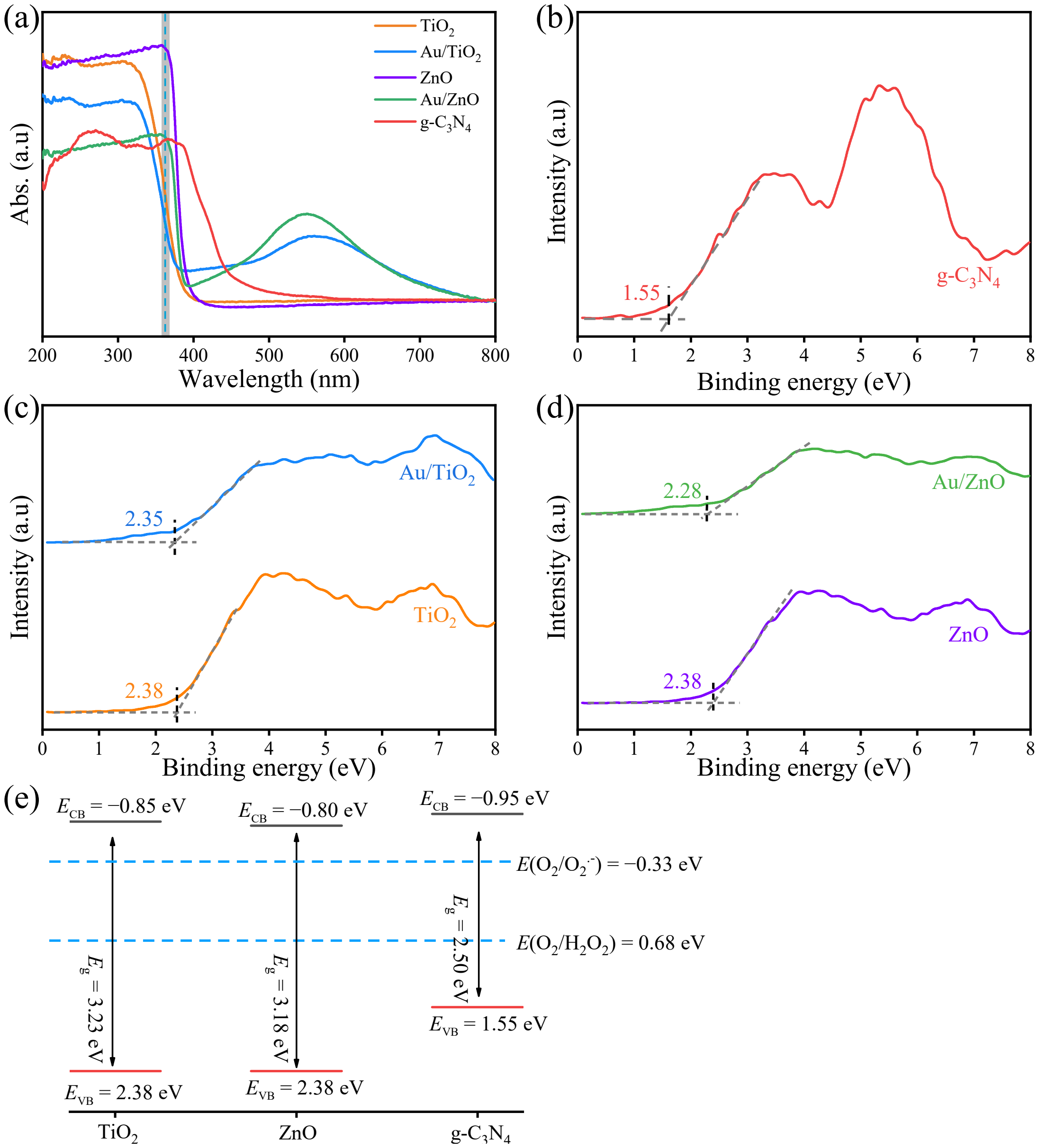

Fig. S7. (a) The UV-vis DRS spectra and (b-d) the XPS valence band spectra of the investigated photocatalysts. (e) The valence band and conduction band potentials and energy band gaps of TiO_2, ZnO, and $g\text{-}C_3N_4$.

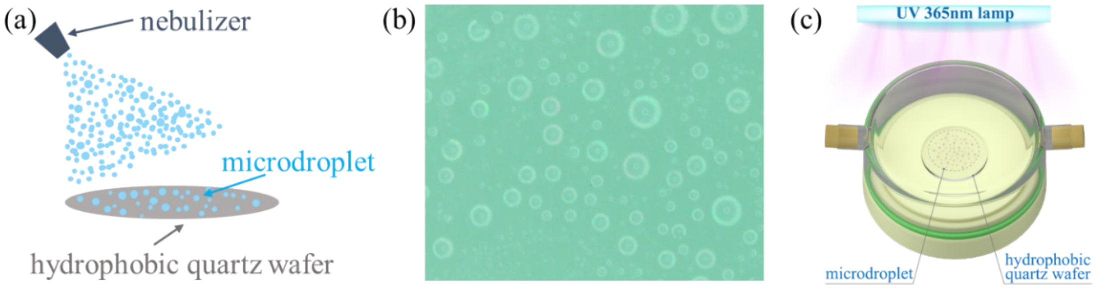

Fig. S8. (a) Schematic illustration of microdroplets generation via nebulizer spraying, (b) graph of the generated microdroplets of varying size, and (c) the custom-designed environmental chamber for microdroplet photocatalysis.

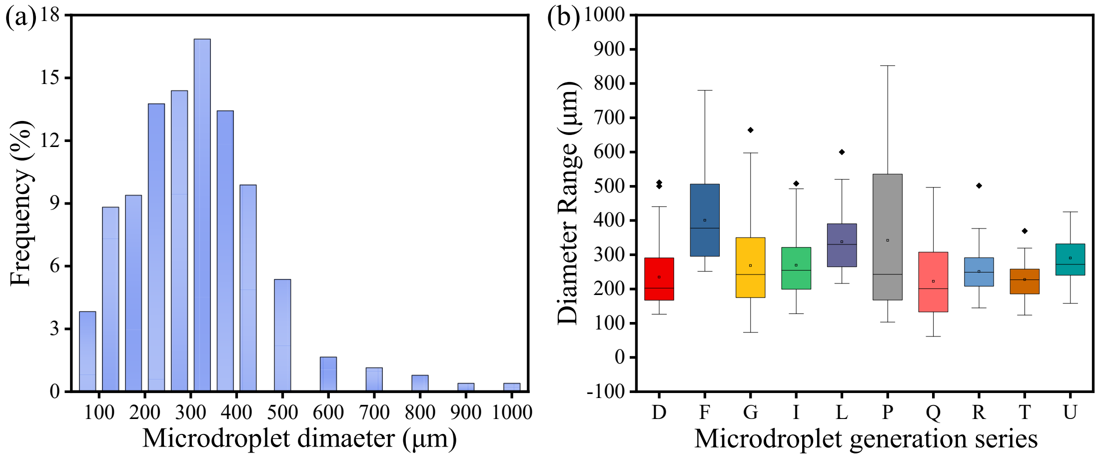

Fig. S9. (a) Distribution histogram of microdroplets diameter generated *via* a homemade nebulizer and (b) repeatability of the microdroplet generation method.

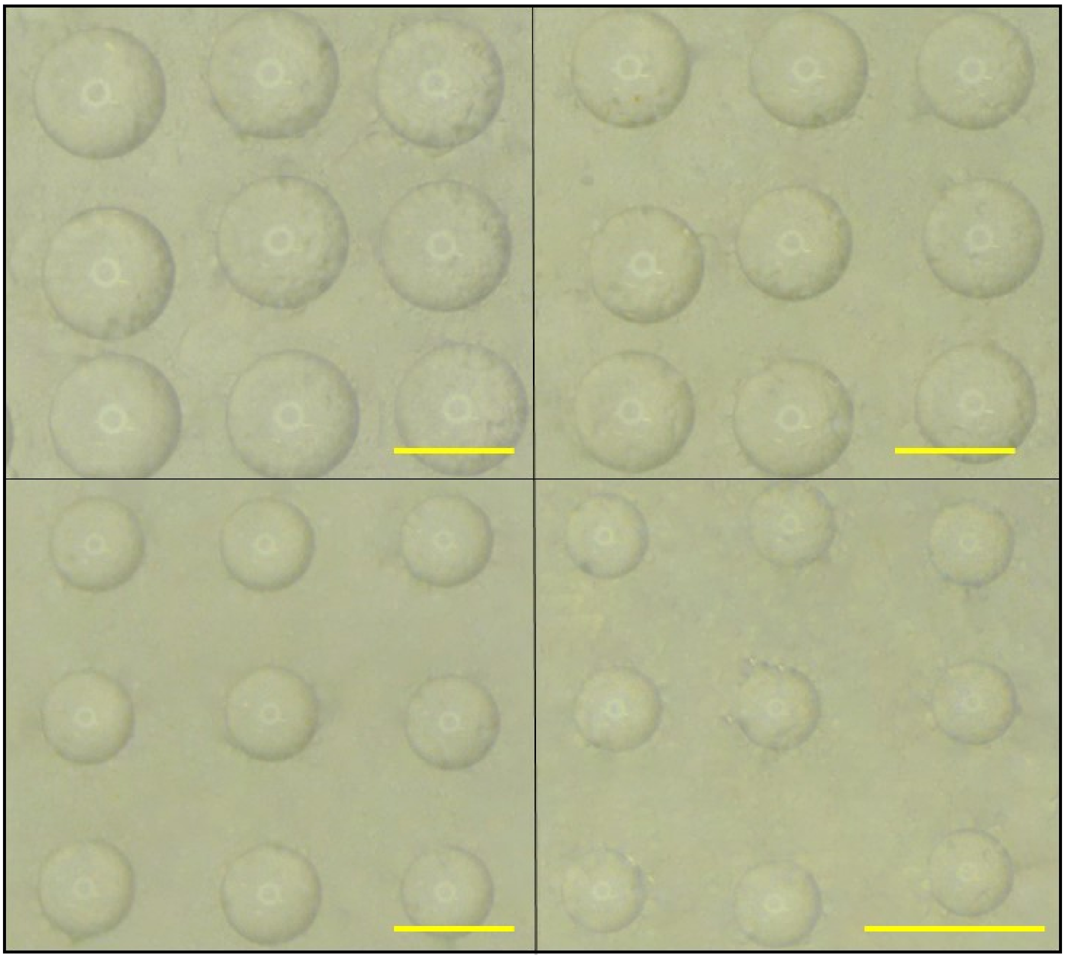

Fig. S10. Images of microdroplet arrays with almost uniform diameter generated using an ink-jet printer from g-C_3N_4 suspension. The scale bar is 400 μm.

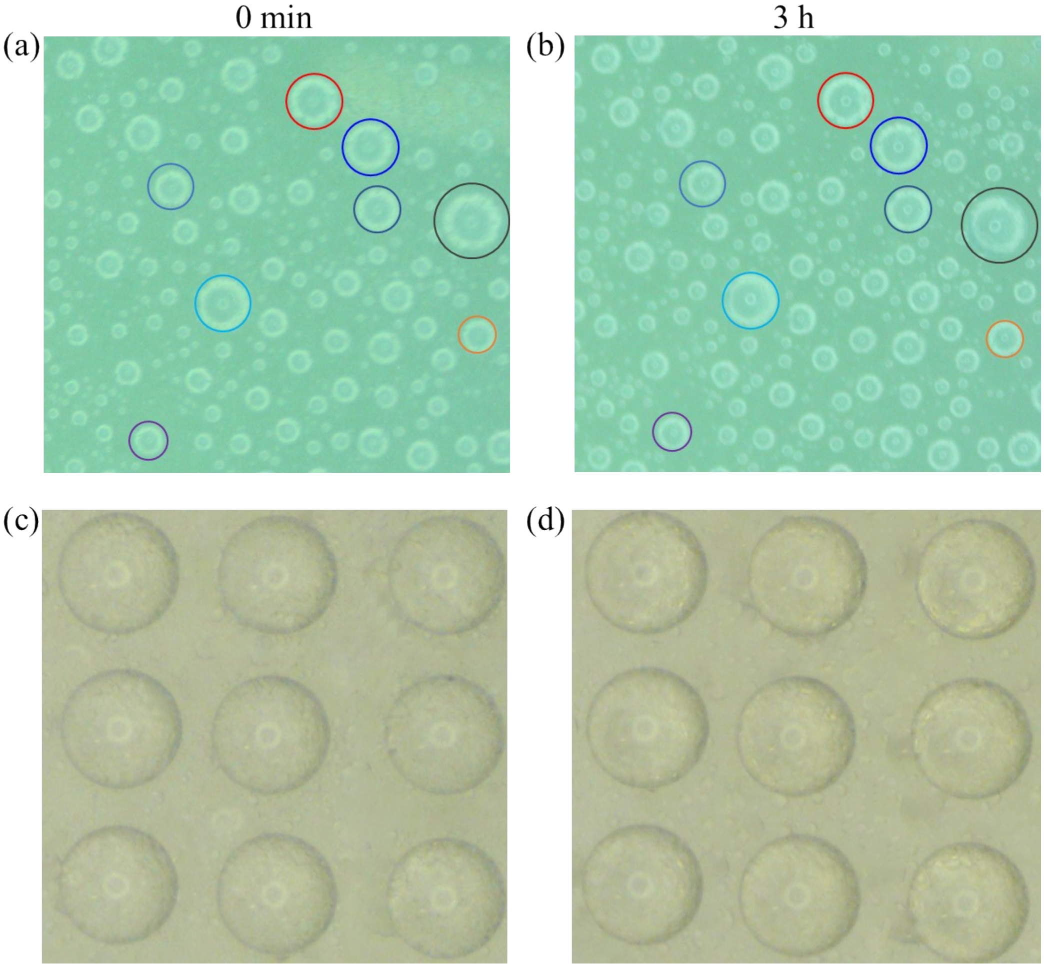

Fig. S11. Photos of microdroplets generated via nebulizer spraying (a and b) and inkjet printing (c and d) before and after photocatalytic reactions (3 h).

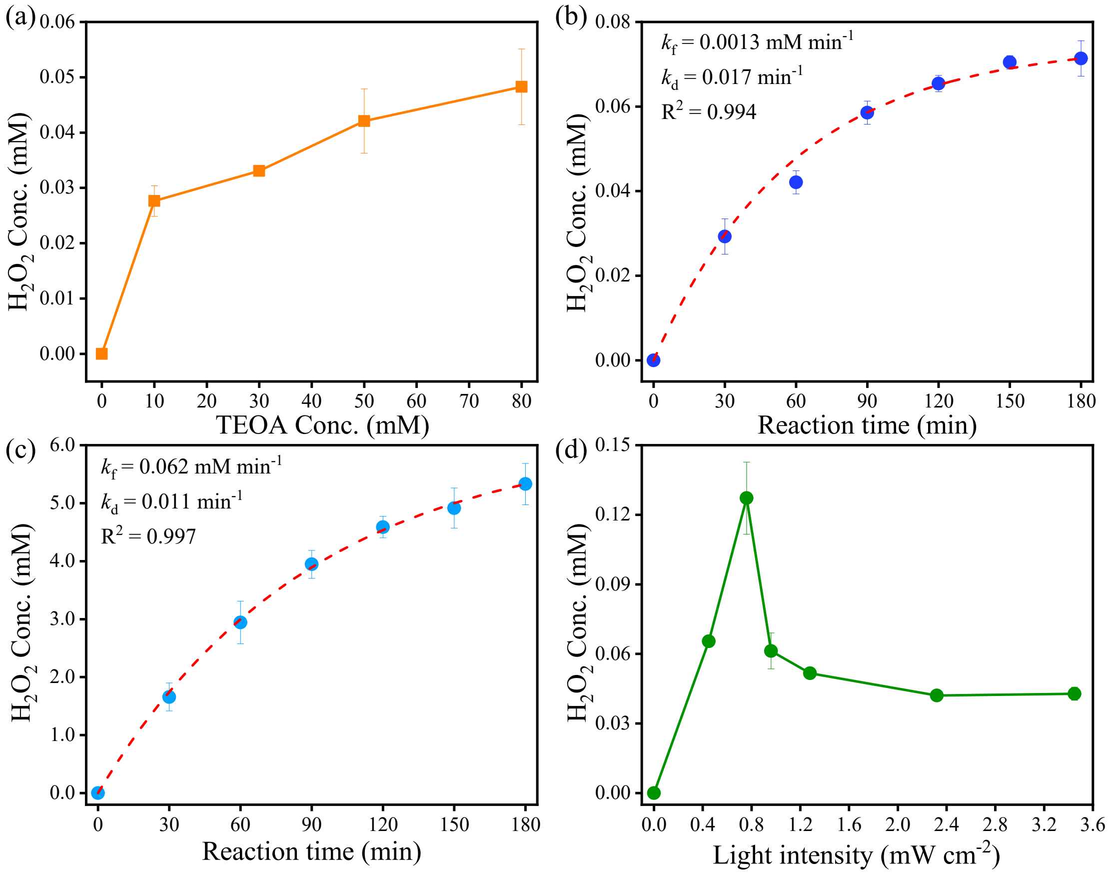

Fig. S12. (a, b, and d) Enlarged versions of photocatalytic H_2O_2 production in bulk phase under different experimental conditions. Kinetics fitting of H_2O_2 photosynthesis relative to the reaction time in (b) bulk phase and (c) microdroplets.

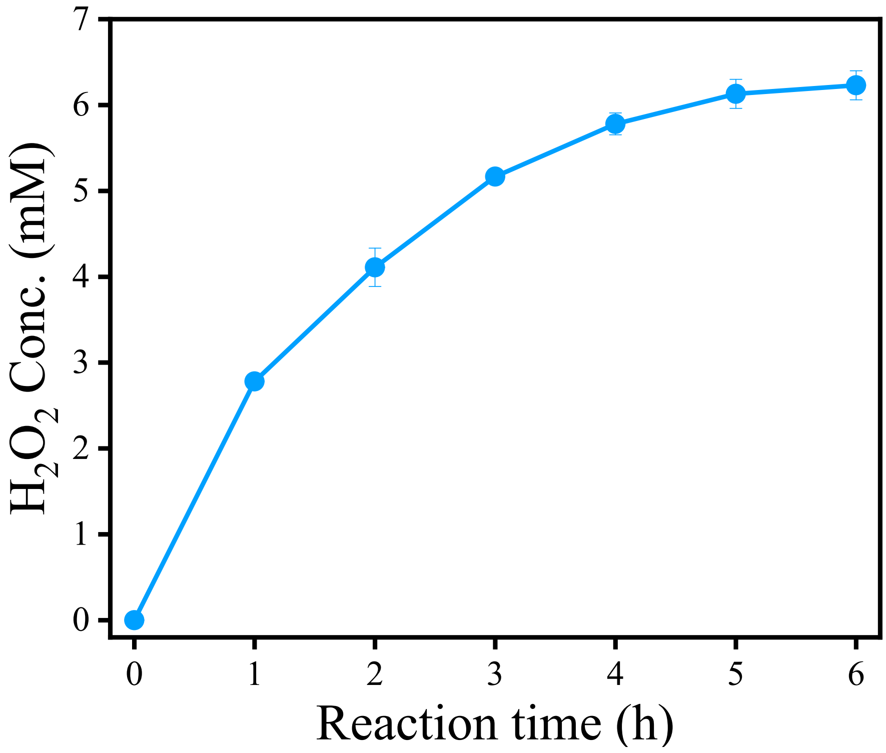

Fig. S13. The long-term tests of microdroplet photocatalytic H_2O_2 production.

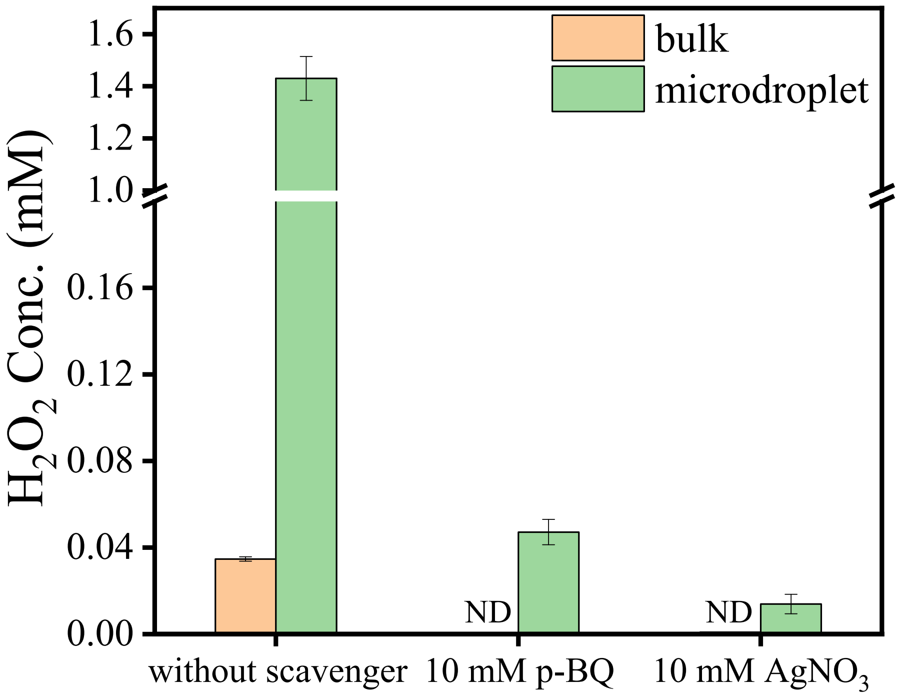

Fig. S14. Photocatalytic H_2O_2 production in bulk solution and microdroplets in the presence of 10 mM p-BQ (a $O_2^{\bullet-}$ radical quencher) and 10 mM $AgNO_3$ (a photoelectrons scavenger). Here, 10 vol.% ethanol was used as holes scavenger because TEOA could react with p-BQ and $AgNO_3$. ND means no detection. Reaction time, 30 min.

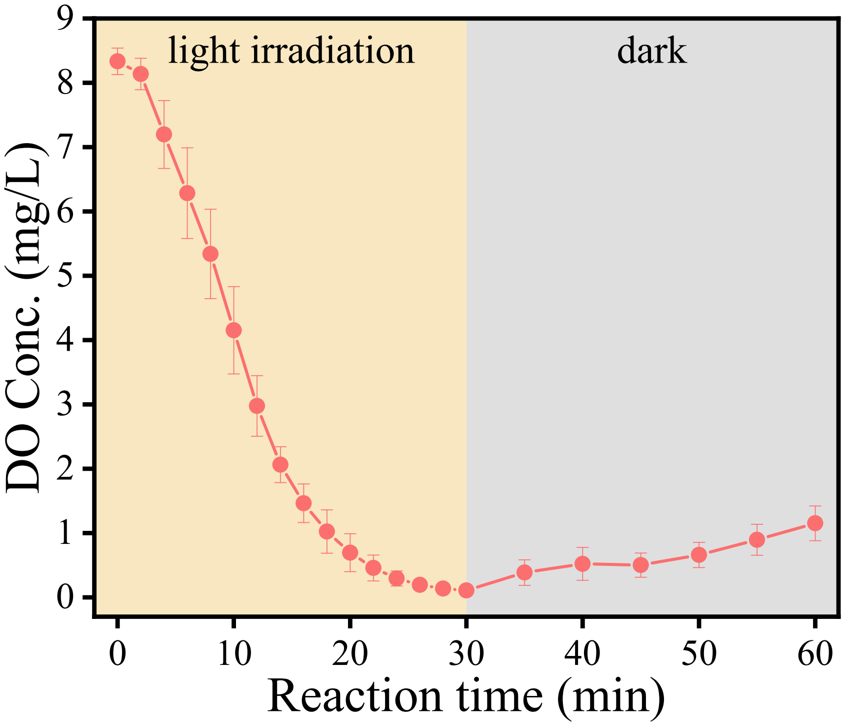

Fig. S15. DO concentration changes during bulk phase photocatalysis without magnetic stirring. The error bars represent the standard deviation of at least three independent repeats.

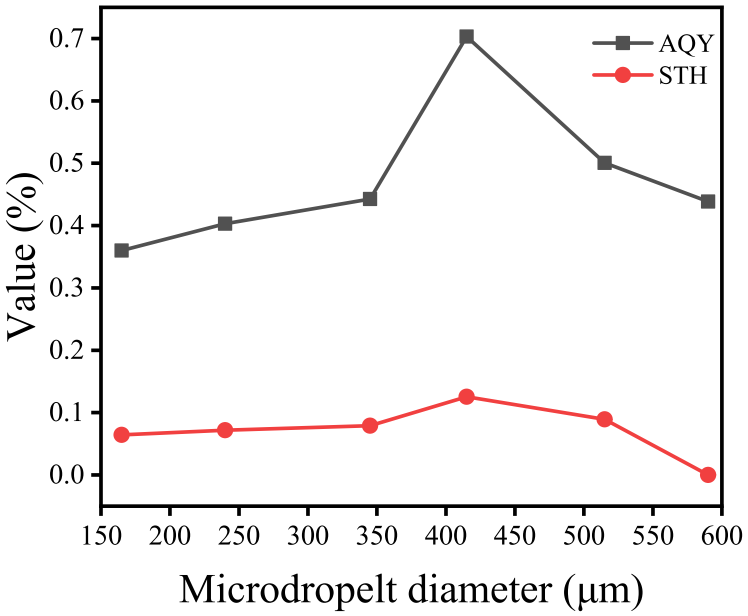

Fig. S16. The AQY and STH of photocatalytic H_2O_2 production in microdroplet of varying diameters.

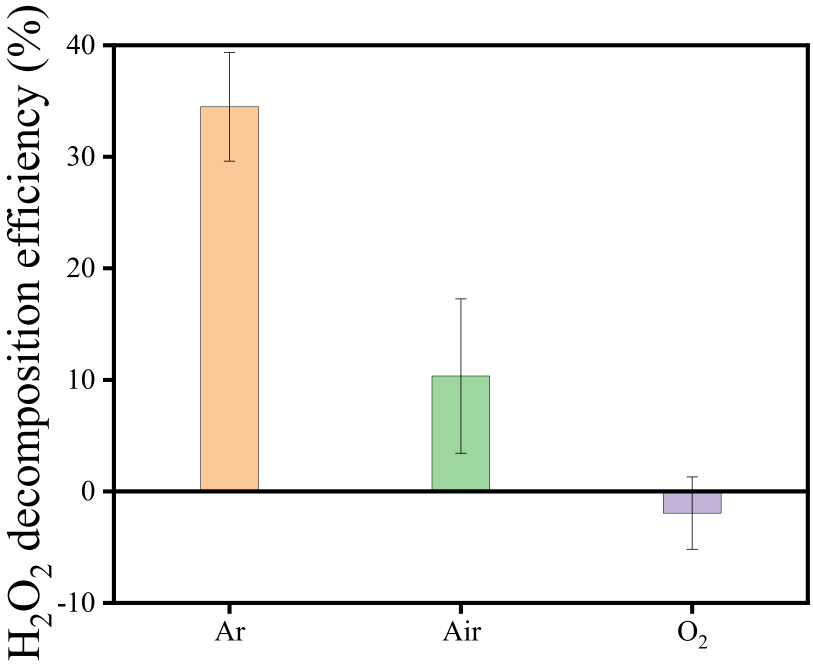

Fig. S17. The photocatalytic H_2O_2 decomposition efficiency in ~160-μm-diameter microdroplet under various reaction atmospheres, where the negative value means that H_2O_2 concentration after photocatalytic reaction was higher than the initial one. Experimental parameters: H_2O_2, 20 mM; TEOA, 50 mM; Reaction time, 1 h. The error bars represent the standard deviation of at least three independent repeats.

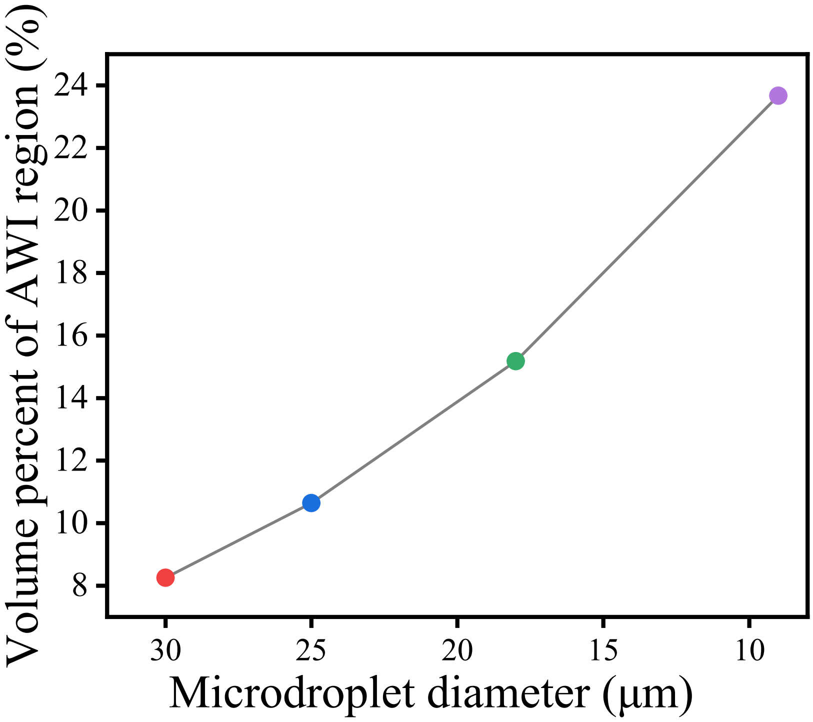

Fig. S18. The volume percent of AWI region in a microdroplet of varying diameter.

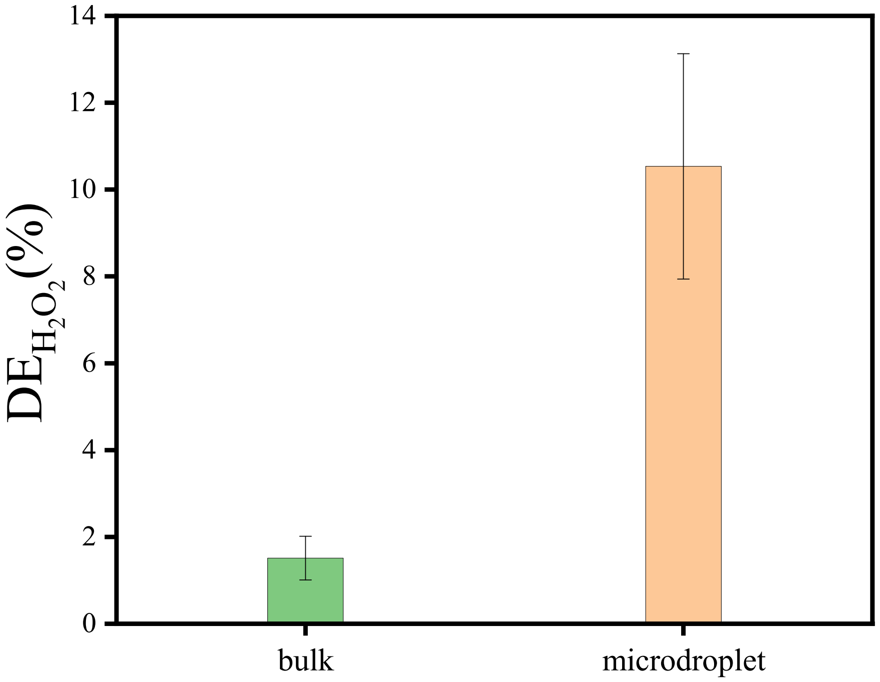

Fig. S19. Photocatalytic H_2O_2 decomposition efficiency ($DE_{H_2O_2}$) in bulk solution and microdroplets under Ar environment using g-C_3N_4 nanosheets as photocatalyst without holes scavenger and magnetic stirring. H_2O_2, 20 mM; Reaction time, 1 h.

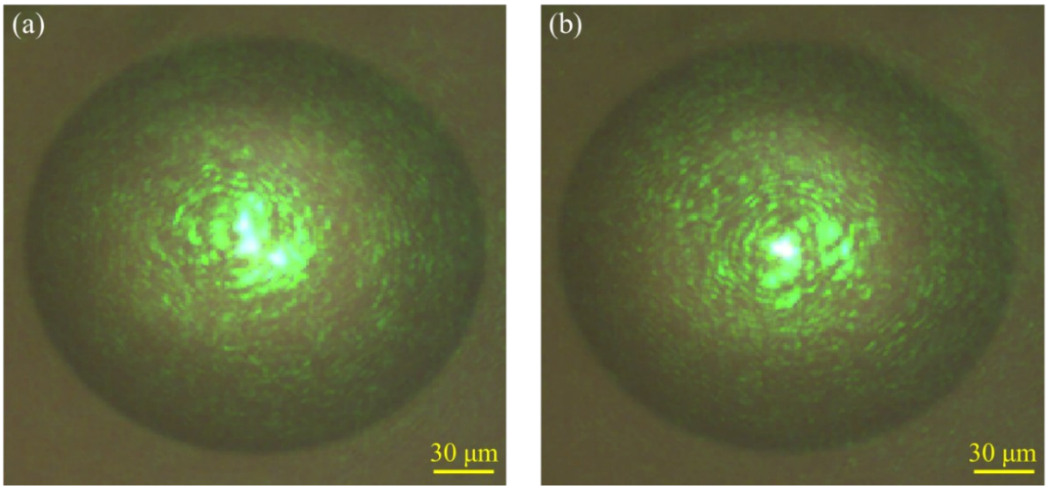

Fig. S20. Micrographs of a microdroplet (a) before and (b) after photocatalytic H_2O_2 decomposition studied by *in-situ* Raman measurement. The green color was caused by 532 nm laser.

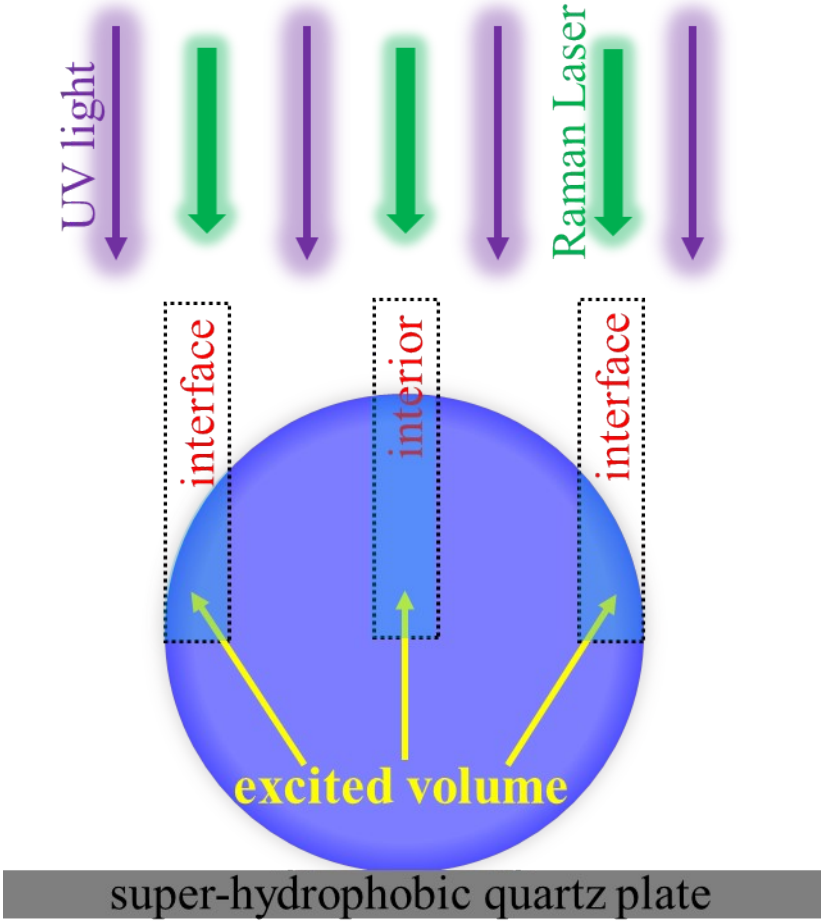

Fig. S21. Schematic illustration of *in-situ* micro-Raman spectroscopy measurements at different regions in a microdroplet during photocatalytic H_2O_2 decomposition. The UV light was off when Raman measurements were performed.

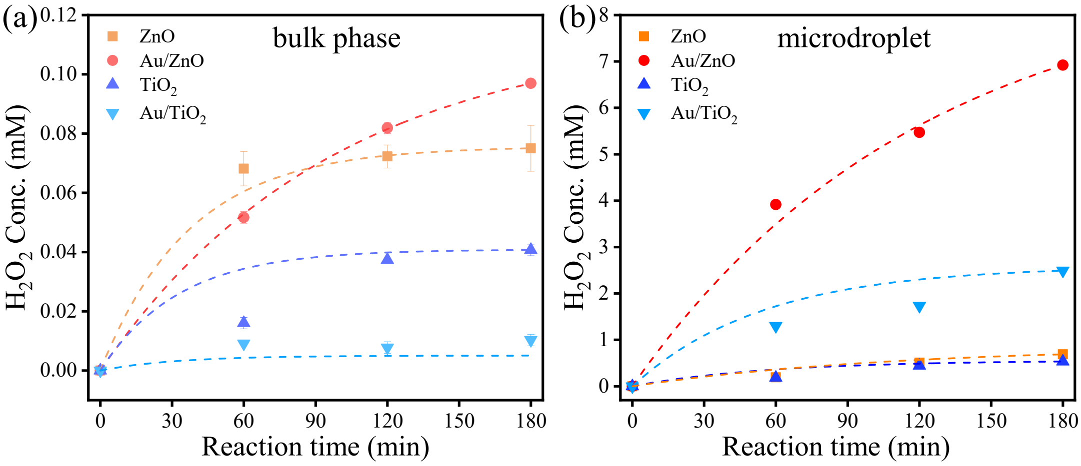

Fig. S22. Kinetics fitting of photocatalytic H_2O_2 production as a function of reaction time in (a) bulk phase and (b) microdroplet with TiO_2, Au/TiO_2, ZnO and Au/ZnO as photocatalysts.

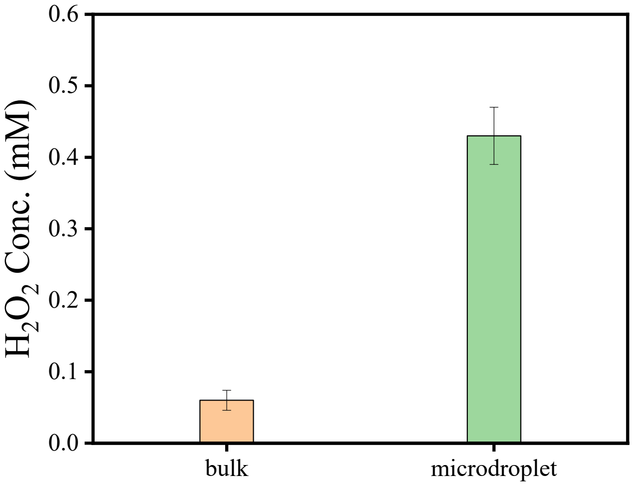

Fig. S23. The H_2O_2 production on Au/ZnO in the absence of TEOA in microdroplet and bulk solution.

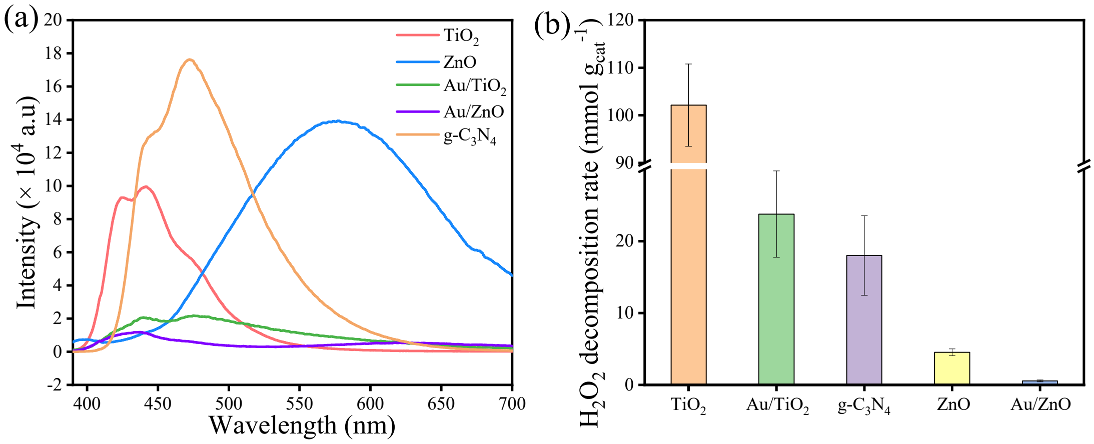

Fig. S24. (a) Photoluminescence spectra of all the employed photocatalysts recorded after sample was excited by a 365 nm light. (b) Photocatalytic H_2O_2 decomposition rate on the five photocatalysts under air condition. Experimental conditions: H_2O_2, 10 mM; TEOA, 10 mM; reaction time, 60 min; magnetic stirring, 300 rpm. The error bars represent the standard deviation of at least three independent repeats.

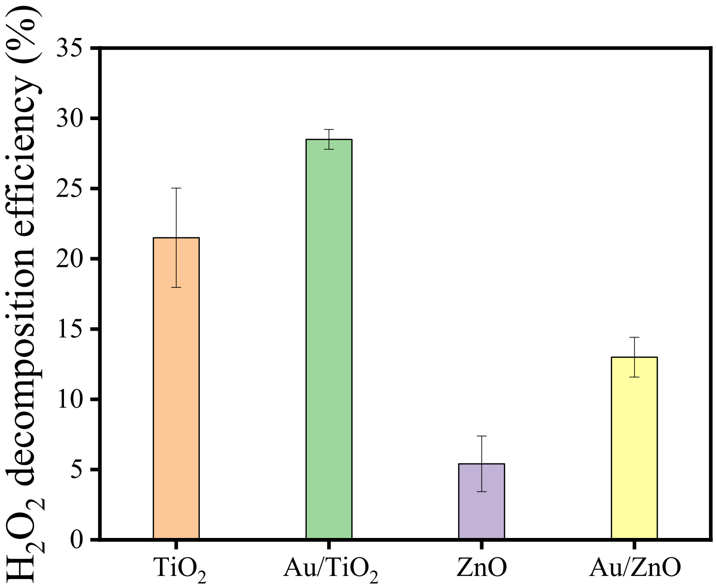

Fig. S25. Photocatalytic H_2O_2 decomposition efficiency in bulk phase on TiO_2, Au/TiO_2, ZnO, and Au/ZnO under Ar atmosphere. Experimental conditions: H_2O_2, 10 mM; TEOA, 10 mM; reaction time, 60 min; magnetic stirring, 300 rpm. The error bars represent the standard deviation of at least two independent repeats.

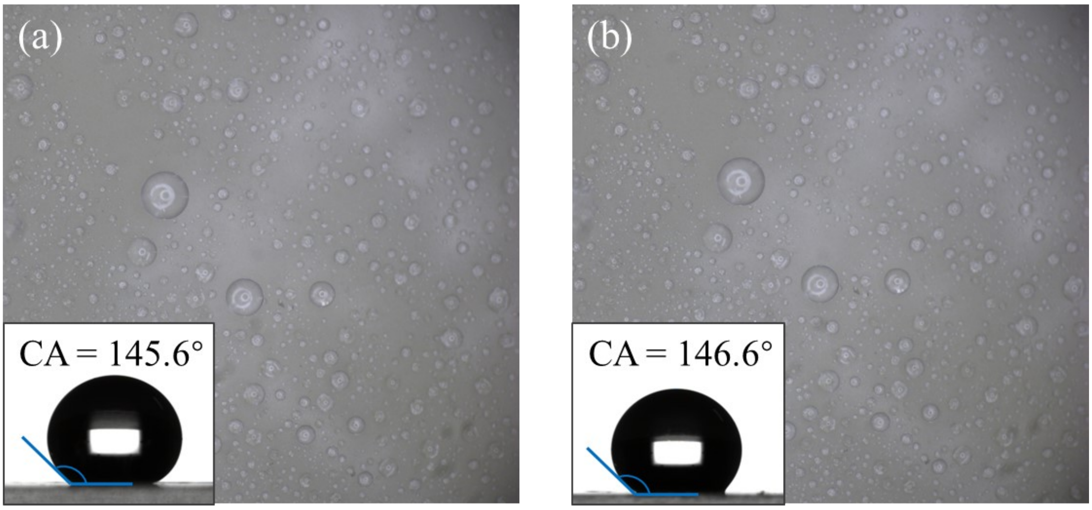

Fig. S26. The micrographs of microdroplets with varying diameters (a) before and (b) after photocatalytic reaction for 6 h. The insets in (a) and (b) are the corresponding water contact angle of superhydrophobic quartz wafer.

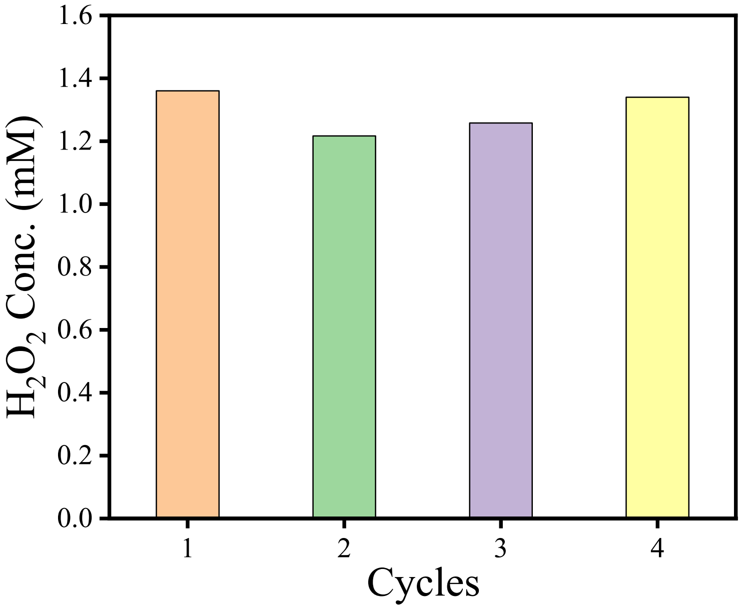

Fig. S27. Repeated photocatalytic H_2O_2 production with g-C_3N_4 in microdroplet photocatalysis system.

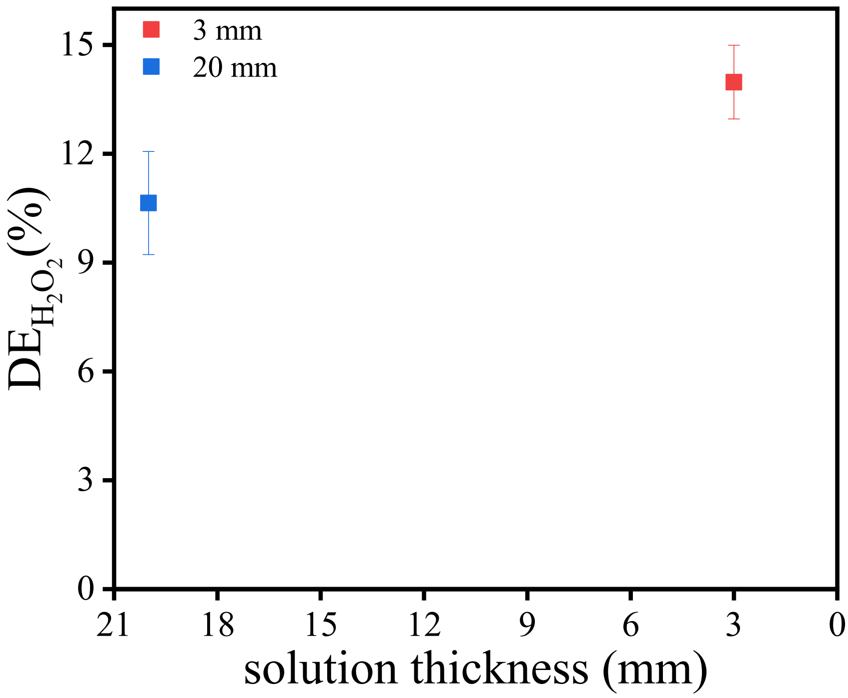

Fig. S28. Photocatalytic H_2O_2 decomposition efficiency ($DE_{H_2O_2}$) on Au/TiO$_2$ under Ar environment in bulk phase with different solution thickness in the absence of holes scavenger. H_2O_2, 20 mM; Reaction time, 1 h.

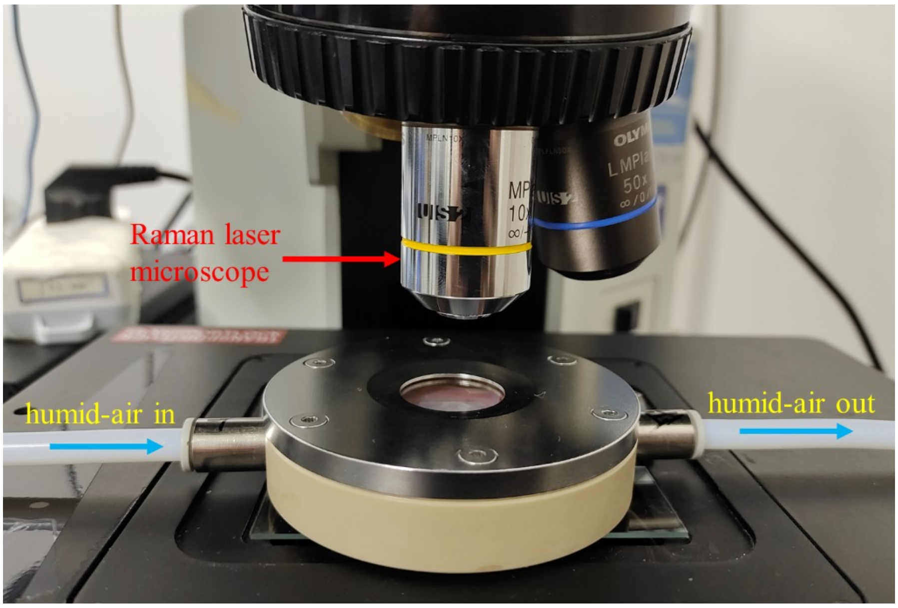

Fig. S29. Custom-designed flow cell for *in-situ* micro-Raman spectroscopy measurements.

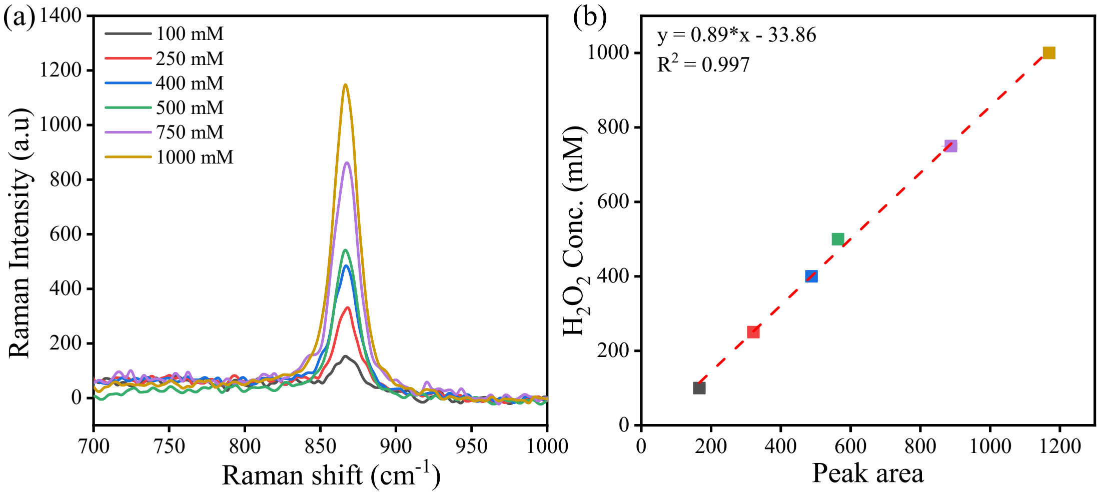

Fig. S30. (a) Raman spectrum of H_2O_2 with different concentrations. (b) Calibration curve for quantitative analysis.

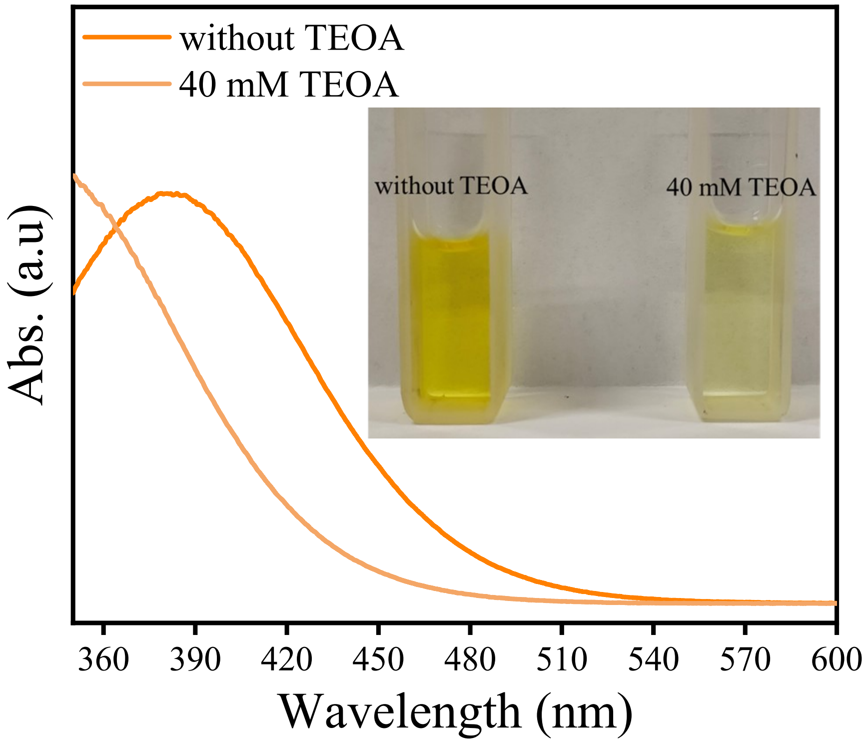

Fig. S31. Effects of TEOA on H_2O_2 detection using PTO and spectroscopic analysis. The inset is photo of tracer liquids in the absence and presence of TEOA.

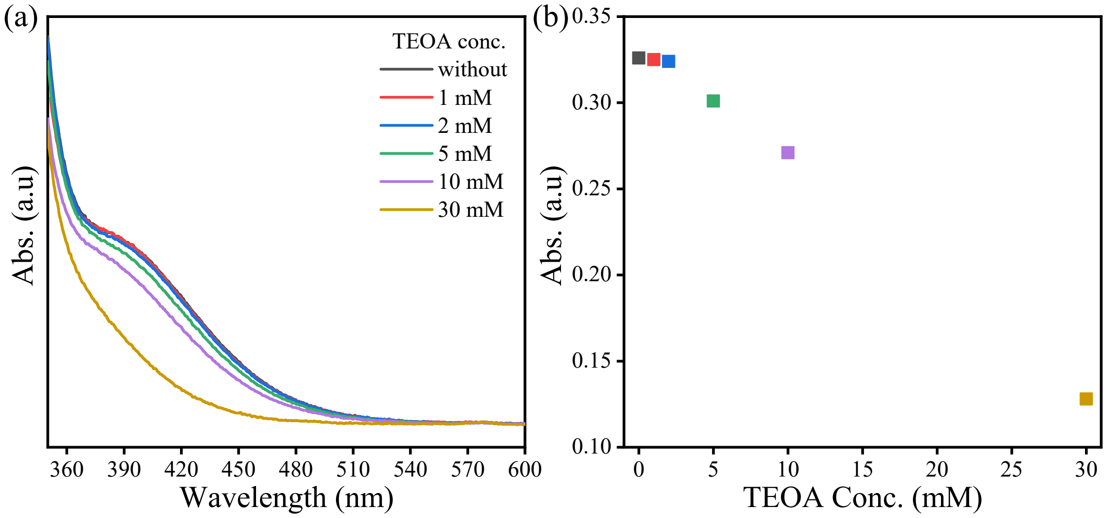

Fig. S32. Influences of TEOA concentrations on H_2O_2 spectroscopic determination. (a) Absorption spectra and (b) absorbance at 400 nm in the presence of TEOA with different concentrations.

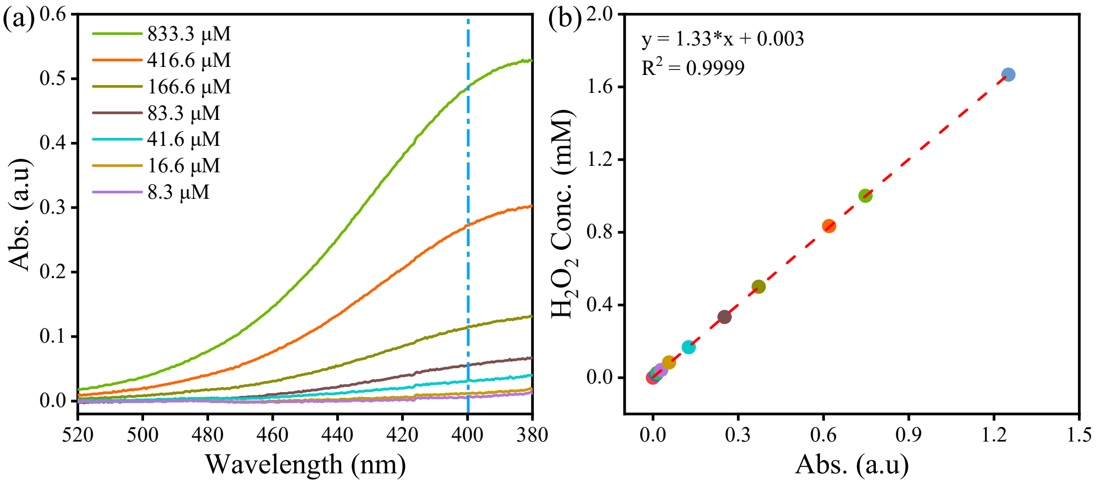

Fig. S33. (a) Absorption spectra of H_2O_2 solution with gradient concentrations in the presence of PTO, and (b) calibration curve for quantitative analysis.

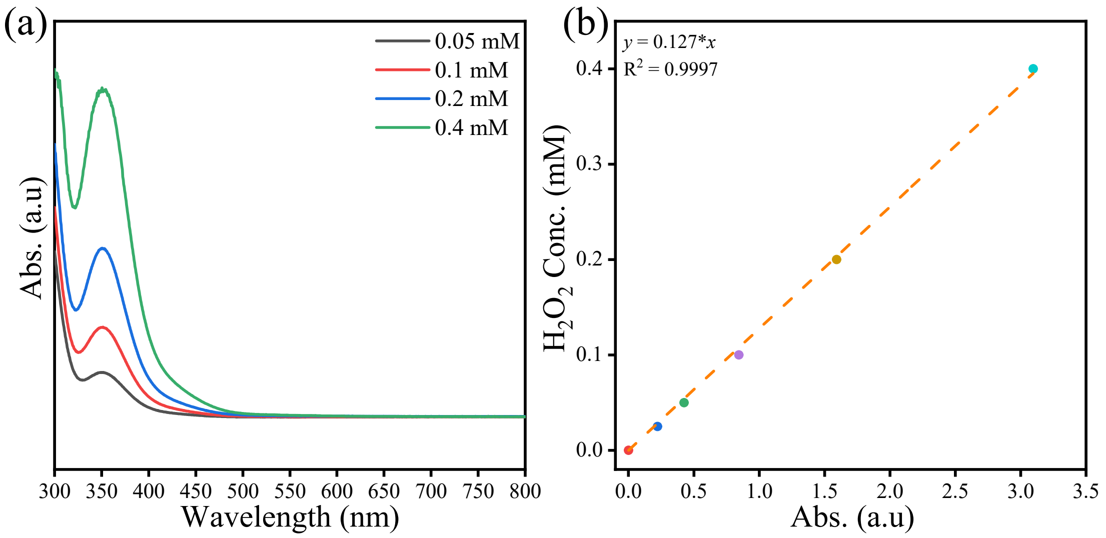

Fig. S34. (a) The UV-vis absorption spectra and (b) established calibration curve for H_2O_2 measurements using KI-$(NH_4)_2MoO_4$ method.

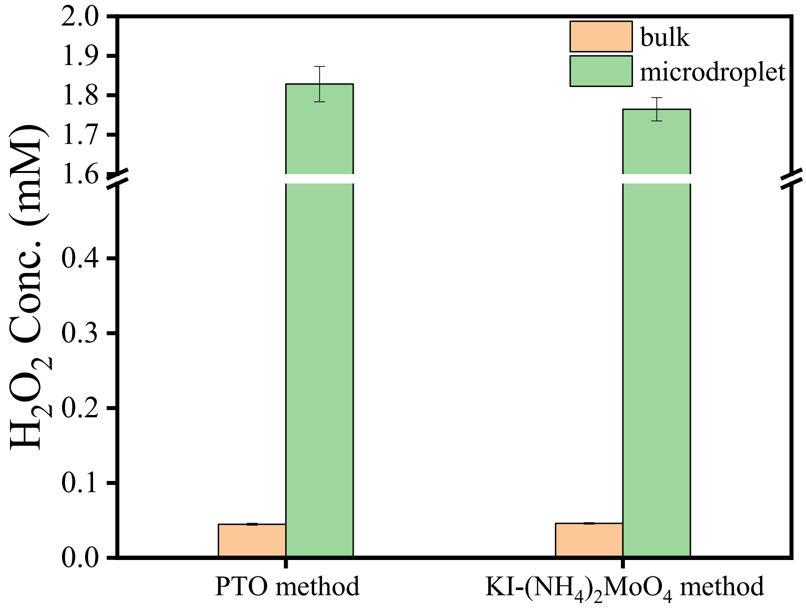

Fig. S35. The measured H_2O_2 concentration after photocatalysis in microdroplet and bulk solution for 1 h, using PTO and KI-$(NH_4)_2MoO_4$ method.

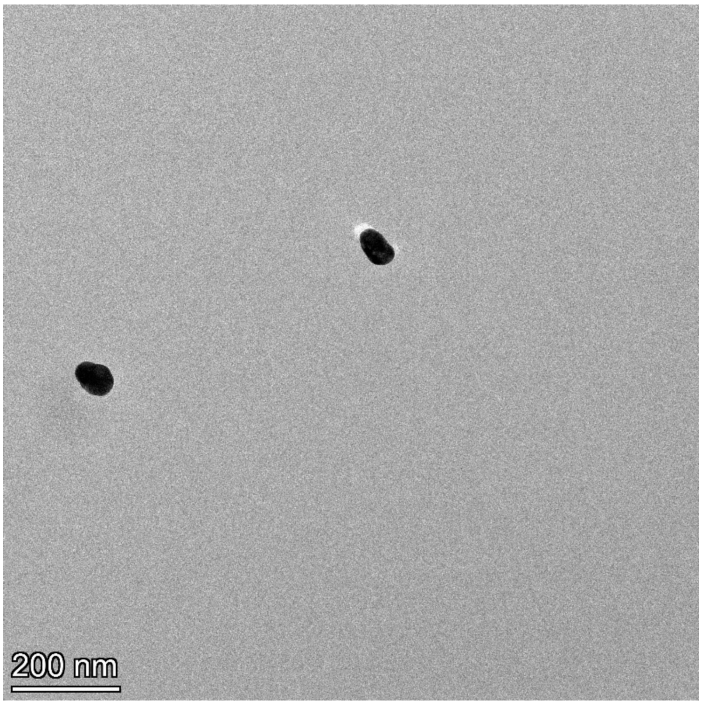

Fig. S36. The TEM image of Au nanoparticles used for vibrational Stark effect measurement.

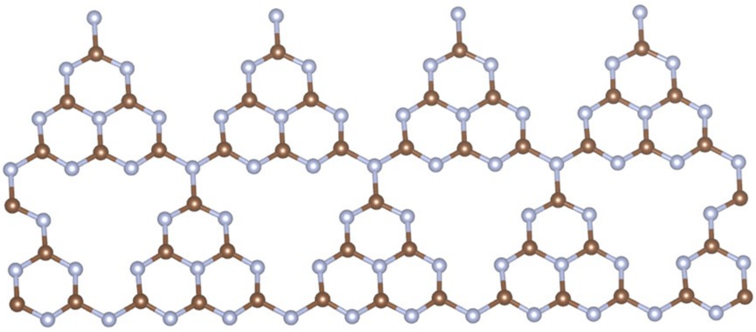

Fig. S37. The supercell of nitrogen-bridged heptazine for DFT calculation.

Table S1. Photocatalytic H_2O_2 formation (k_f) and decomposition (k_d) rate constants obtained in bulk solution and microdroplets on different photocatalysts.

	k_f/mM min^{-1}		k_d/min^{-1}	
	bulk	microdroplet	bulk	microdroplet
g-C_3N_4	0.0013	0.062	0.017	0.011
ZnO	0.002	0.007	0.026	0.009
Au/ZnO	0.001	0.072	0.01	0.008
TiO_2	0.001	0.009	0.03	0.017
Au/TiO_2	0.0003	0.046	0.031	0.018

Table S2. The comparisons of photocatalytic H_2O_2 production rates.

photocatalyst	*holes scavenger*	*reaction time (h)*	*H_2O_2 evolution rate (mmol g^{-1} h^{-1})*	*Ref.*
g-C_3N_4	*50 mM TEOA*	*3*	*20.6*	*This work*
TiO_2			*0.62*	
Au/TiO_2			*9.23*	
ZnO			*0.53*	
Au/ZnO			*13.6*	
CN-OH	37 vol.% EtOH	1	18.2	21
OPA/$Zr_{92.5}Ti_{7.5}$-MOF	250 vol.% BA	3	13.6	22
S,K co-doped g-C_3N_4	10 vol.% EtOH	3	2.73	23
RF/P_3HT-1.0	–	5	0.62	24
BP/CN	10 vol.% IPA	1	0.54	25
$Cu_2(OH)$-PO_4/g-C_3N_4	–	4	1.8	26
$Au_{0.1}Ag_{0.4}/TiO_2$	4 vol.% EtOH	12	0.28	27
SRF-250	–	1	1.17	28
PM-CDs-30	–	5	1.76	29
Sb-SAPC	–	6	0.29	30
Co_1/AQ/ g-C_3N_4	–	1	0.12	31
GCN	10 vol.% EtOH	24	0.19	32
PEI/g-C_3N_4	–	4	0.29	33
KPD-CN-7.5	10 vol.% EtOH	12	0.46	34
$PI_{5.0}$-NCN	–	2	1.15	35
rGO/TiO_2	5 vol% of 2-propanol	3	3	36
C_3N_4-carbon	5 vol% of 2-propanol	4	1.27	37
α-Fe_2O_3/CQD@g-C_3N_4	–	1	0.14	38
OCN-500	5 vol% of 2-propanol	5	1.2	39
CPN	–	8	1.97	40
Au/ZnO	4 vol.% EtOH	12	1.53	41
ZIF-8/g-C_3N_4	–	10	2.64	42
SnS_2/In_2S_3/CDs	–	3	1.12	43
CTF-NS-5BT	10 vol.% BA	2	1.63	44
Nv-C≡N-CN	10 vol.% IPA	1	3.93	45
CoOx/Mo:$BiVO_4$/Pd	–	1	8.4	18
10% ZnO/g-C_3N_4	10 vol.% EtOH	8	0.66	46
PLCN-30	0.8 g L^{-1} EtOH	4	0.95	47

References

1. D. Zhao, Y. Wang, C.-L. Dong, Y.-C. Huang, J. Chen, F. Xue, S. Shen and L. Guo, *Nat. Energy*, 2021, **6**, 388-397.
2. P. Niu, L. Zhang, G. Liu and H.-M. Cheng, *Adv. Funct. Mater.*, 2012, **22**, 4763-4770.
3. Y. Wang, Y. Wang, J. Zhao, M. Chen, X. Huang and Y. Xu, *Appl. Catal. B Environ.*, 2021, **284**, 119691.
4. C. Wang, C. Tan, W. Lv, G. Zhu, Z. Wei, K. H. L. Zhang and W. He, *Mater. Today Chem.*, 2018, **8**, 36-41.
5. J. Hu, C. Chen, H. Yang, F. Yang, J. Qu, X. Yang, W. Sun, L. Dai and C. M. Li, *Appl. Catal. B Environ.*, 2022, **317**, 121723.
6. G. O. Rabell, M. R. A. Cruz and I. Juárez-Ramírez, *Mater. Sci. Semicond. Process.*, 2021, **134**, 105985.
7. J. K. Lee, K. L. Walker, H. S. Han, J. Kang, F. B. Prinz, R. M. Waymouth, H. G. Nam and R. N. Zare, *Proc. Natl. Acad. Sci. U. S. A.*, 2019, **116**, 19294-19298.
8. L. Zhou, J. Lei, F. Wang, L. Wang, M. R. Hoffmann, Y. Liu, S.-I. In and J. Zhang, *Appl. Catal. B-Environ.*, 2021, **288**, 119993.
9. H. Xiong, J. K. Lee, R. N. Zare and W. Min, *J. Phys. Chem. Lett.*, 2020, **11**, 7423-7428.
10. H. Shi, Z. Cai, J. Patrow, B. Zhao, Y. Wang, Y. Wang, A. Benderskii, J. Dawlaty and S. B. Cronin, *ACS Appl. Mater. Interfaces*, 2018, **10**, 33678-33683.
11. B. Ren, Q.-J. Huang, Y. Xie and Z.-Q. Tian, *Anal. Sci.*, 2000, **16**, 225-230.
12. G. Cabello, X.-J. Chen, R. Panneerselvam and Z.-Q. Tian, *J. Raman Spectrosc.*, 2016, **47**, 1207-1212.
13. L. Xie, J. Lu, T. Liu, G. Chen, G. Liu, B. Ren and Z. Tian, *J. Phys. Chem. Lett.*, 2020, **11**, 1022-1029.
14. I. Nam, H. G. Nam and R. N. Zare, *Proc. Natl. Acad. Sci. U. S. A.*, 2018, **115**, 36-40.
15. Y. Zhao, P. Zhang, Z. Yang, L. Li, J. Gao, S. Chen, T. Xie, C. Diao, S. Xi and B. Xiao, *Nat. Commun.*, 2021, **12**, 1-11.
16. H. Che, X. Gao, J. Chen, J. Hou, Y. Ao and P. Wang, *Angew. Chem. Int. Ed.*, 2021, **60**, 25546-25550.
17. W. Liu, P. Wang, J. Chen, X. Gao, H. Che, B. Liu and Y. Ao, *Adv. Funct. Mater.*, 2022, **32**, 2205119.
18. T. Liu, Z. Pan, J. J. M. Vequizo, K. Kato, B. Wu, A. Yamakata, K. Katayama, B. Chen, C. Chu and K. Domen, *Nat. Commun.*, 2022, **13**, 1034.
19. L. Li, L. Xu, Z. Hu and J. C. Yu, *Adv. Funct. Mater.*, 2021, **31**, 2106120.
20. C. F. Chamberlayne and R. N. Zare, *J Chem. Phys.*, 2020, **152**, 184702.
21. W. Hou, Y. Li, S. Ouyang, H. Chen, J. Ye, X. Han and Y. Deng, *Chem. Commun.*, 2019, **55**, 13279-13282.
22. Y. Isaka, Y. Kawase, Y. Kuwahara, K. Mori and H. Yamashita, *Angew. Chem. Int. Ed.*, 2019, **58**, 5402-

5406.

23. P. Zhang, Y. Tong, Y. Liu, J. J. M. Vequizo, H. Sun, C. Yang, A. Yamakata, F. Fan, W. Lin, X. Wang and W. Choi, *Angew. Chem. Int. Ed.*, 2020, **59**, 16209-16217.

24. Y. Shiraishi, M. Matsumoto, S. Ichikawa, S. Tanaka and T. Hirai, *J. Am. Chem. Soc.*, 2021, **143**, 12590-12599.

25. Y. Zheng, Z. Yu, H. Ou, A. M. Asiri, Y. Chen and X. Wang, *Adv. Funct. Mater.*, 2018, **28**, 1705407.

26. X. Wang, Z. Han, L. Yu, C. Liu, Y. Liu and G. Wu, *ACS Sustain. Chem. Eng.*, 2018, **6**, 14542-14553.

27. D. Tsukamoto, A. Shiro, Y. Shiraishi, Y. Sugano, S. Ichikawa, S. Tanaka and T. Hirai, *ACS Catal.*, 2012, **2**, 599-603.

28. L. Yuan, C. Zhang, J. Wang, C. Liu and C. Yu, *Nano Res.*, 2021, **14**, 3267-3273.

29. Q. Wu, J. Cao, X. Wang, Y. Liu, Y. Zhao, H. Wang, Y. Liu, H. Huang, F. Liao, M. Shao and Z. Kang, *Nat. Commun.*, 2021, **12**, 483.

30. Z. Teng, Q. Zhang, H. Yang, K. Kato, W. Yang, Y.-R. Lu, S. Liu, C. Wang, A. Yamakata, C. Su, B. Liu and T. Ohno, *Nat. Catal.*, 2021, **4**, 374-384.

31. C. Chu, Q. Zhu, Z. Pan, S. Gupta, D. Huang, Y. Du, S. Weon, Y. Wu, C. Muhich, E. Stavitski, K. Domen and J.-H. Kim, *Proc. Natl. Acad. Sci. U. S. A.*, 2020, **117**, 6376-6382.

32. Y. Shiraishi, Y. Kofuji, H. Sakamoto, S. Tanaka, S. Ichikawa and T. Hirai, *ACS Catal.*, 2015, **5**, 3058-3066.

33. X. Zeng, Y. Liu, Y. Kang, Q. Li, Y. Xia, Y. Zhu, H. Hou, M. H. Uddin, T. R. Gengenbach, D. Xia, C. Sun, D. T. McCarthy, A. Deletic, J. Yu and X. Zhang, *ACS Catal.*, 2020, **10**, 3697-3706.

34. G.-h. Moon, M. Fujitsuka, S. Kim, T. Majima, X. Wang and W. Choi, *ACS Catal.*, 2017, **7**, 2886-2895.

35. L. Yang, G. Dong, D. L. Jacobs, Y. Wang, L. Zang and C. Wang, *J. Catal.*, 2017, **352**, 274-281.

36. G.-h. Moon, W. Kim, A. D. Bokare, N.-e. Sung and W. Choi, *Energy Environ. Sci.*, 2014, **7**, 4023-4028.

37. R. Wang, X. Zhang, F. Li, D. Cao, M. Pu, D. Han, J. Yang and X. Xiang, *J. Energy. Chem.*, 2018, **27**, 343-350.

38. X. Chen, W. Zhang, L. Zhang, L. Feng, C. Zhang, J. Jiang, T. Yan and H. Wang, *J. Mater. Chem. A*, 2020, **8**, 18816-18825.

39. Z. Wei, M. Liu, Z. Zhang, W. Yao, H. Tan and Y. Zhu, *Energy Environ. Sci.*, 2018, **11**, 2581-2589.

40. J. Cao, H. Wang, Y. Zhao, Y. Liu, Q. Wu, H. Huang, M. Shao, Y. Liu and Z. Kang, *J. Mater. Chem. A*, 2020, **8**, 3701-3707.

41. X. Meng, P. Zong, L. Wang, F. Yang, W. Hou, S. Zhang, B. Li, Z. Guo, S. Liu, G. Zuo, Y. Du, T. Wang and

V. A. L. Roy, *Catal. Commun.*, 2020, **134**, 105860.

42. Y. Zhao, Y. Liu, J. Cao, H. Wang, M. Shao, H. Huang, Y. Liu and Z. Kang, *Appl. Catal. B Environ.*, 2020, **278**, 119289.
43. Y. Li, Y. Zhao, H. Nie, K. Wei, J. Cao, H. Huang, M. Shao, Y. Liu and Z. Kang, *J. Mater. Chem. A*, 2021, **9**, 515-522.
44. X. Yu, B. Viengkeo, Q. He, X. Zhao, Q. Huang, P. Li, W. Huang and Y. Li, *Adv. Sustain. Syst.*, 2021, **5**, 2100184.
45. X. Zhang, P. Ma, C. Wang, L. Gan, X. Chen, P. Zhang, Y. Wang, H. Li, L. Wang, X. Zhou and K. Zheng, *Energy Environ. Sci.*, 2022, **15**, 830-842.
46. X. Geng, L. Wang, L. Zhang, H. Wang, Y. Peng and Z. Bian, *Chem. Eng. J.*, 2021, **420**, 129722.
47. X. Li, J. Zhang, F. Zhou, H. Zhang, J. Bai, Y. Wang and H. Wang, *Chinese J. Catal.*, 2018, **39**, 1090-1098.